2013

Tensile testing of individual glassy, rubbery and hydrogel electrospun polymer nanofibres to high strain using the atomic force microscope

Adrian Gestos
University of Wollongong, gestos@uow.edu.au

Philip G. Whitten
University of Wollongong, whitten@uow.edu.au

Geoffrey M. Spinks
University of Wollongong, gspinks@uow.edu.au

Gordon G. Wallace
University of Wollongong, gwallace@uow.edu.au

Publication Details

Gestos, A., Whitten, P. G., Spinks, G. M. & Wallace, G. G. (2013). Tensile testing of individual glassy, rubbery and hydrogel electrospun polymer nanofibres to high strain using the atomic force microscope. Polymer Testing, 32 (4), 655-664.

Tensile testing of individual glassy, rubbery and hydrogel electrospun polymer nanofibres to high strain using the atomic force microscope

Abstract
The production and use of polymer nanofibre assemblies prepared by electrospinning is now widespread. It is known that the tensile properties of electrospun polymer fibres can be different to those of bulk polymers. Here, we report a general method for measuring the tensile properties of individual electrospun nanofibres that employs a commercial atomic force microscope. Methods for preparing samples, force calibration and calculation of tensile stress and strain are described along with error estimation. By appropriate choice of AFM cantilever, it is shown that the tensile stress-strain curves can be measured for glassy, rubbery and gel polymer nanofibres. Testing can be in air or fluid and to strains of 300%. Example results illustrate the usefulness of the technique with the observation of high ductility in normally brittle glassy polymers such as polystyrene, and unusually large hysteresis in thermoplastic elastomer nanofibres. These observations provide new insights into the structure and mechanical behaviour of nanoscale polymeric materials.

Keywords
atomic, glassy, rubbery, strain, high, nanofibres, polymer, electrospun, force, hydrogel, tensile, testing, microscope, individual

Disciplines
Engineering | Physical Sciences and Mathematics

Publication Details
Gestos, A., Whitten, P. G., Spinks, G. M. & Wallace, G. G. (2013). Tensile testing of individual glassy, rubbery and hydrogel electrospun polymer nanofibres to high strain using the atomic force microscope. Polymer Testing, 32 (4), 655-664.

Tensile testing of individual glassy, rubbery and hydrogel polymer nanofibres to high strain using the atomic force microscope.

Authors

Adrian Gestos[a], Philip G. Whitten[b], Geoffrey M. Spinks[a], Gordon G. Wallace[a]

a. Intelligent Polymer Research Institute, ARC Centre of Excellence for Electromaterials Science, AIIM Facility, Innovation Campus, University of Wollongong, Wollongong, NSW 2522 Australia.

b. School of Mechanical, Materials and Mechatronic Engineering, Faculty of Engineering, University of Wollongong, Wollongong, NSW 2522 Australia.

Abstract

The production and use of polymer nanofibre assemblies prepared by electrospinning is now widespread. It is known that the tensile properties of electrospun polymer fibres can be different to those of bulk polymers. Here we report a general method for measuring the tensile properties of individual electrospun nanofibres that employs a commercial atomic force microscope. Methods for preparing samples, force calibration and calculation of tensile stress and strain are described along with error estimation. By appropriate choice of AFM cantilever, it is shown that the tensile stress-strain curves can be measured for glassy, rubbery and gel polymer nanofibres. Testing can be in air or fluid and to strains of 300%. Example results illustrate the usefulness of the technique with the observation of high ductility in normally brittle glassy polymers such as polystyrene and unusually large hysteresis in thermoplastic elastomer nanofibres. These observations provide new insights into the structure and mechanical behaviour of nanoscale polymeric materials.

Keywords: Mechanical properties; nanofibres; atomic force microscopy; tensile testing

1 Introduction

There is considerable interest in the production of polymers as nanofibres with applications ranging from bioengineering applications[1–6] such as wound dressings,[7] tissue engineering scaffolds,[8–11] and implantable drug delivery membranes[12] to energy applications such as high surface area electrodes in fuel cells,[13] photovoltaics[14] or batteries[15, 16] to water treatment applications as membranes[17, 18] and functionalised filters.[19, 20] In nearly all of these applications the mechanical properties of both the polymer nanofibres, and their assemblies, are important. The nanofibres require a minimum strength for handling and use, and in some cases, such as tissue engineering, the Young's modulus needs to be tailored to a specific range. The mechanical properties of the polymer nanofibre assemblies in the form of macro-scale mats are readily investigated using traditional testing methods.[18, 21–25] However, mechanical tests on nanofibre assemblies are dominated by the strength of interfibre junctions, the radius of curvature of the fibres and the alignment of fibres with the observed properties vastly different to the properties of individual fibres.[26, 27] Appreciation of the mechanical properties of isolated electrospun polymer fibres is an emerging field.

A variety of methods have been developed for mechanical testing of individual polymer nanofibres[28] but so far, no single 'best' approach has emerged. The existing methods range from the use of commercial universal testing machines,[29–31] to microelectronic mechanical systems (MEMS)[32–35] and the use of atomic force microscope (AFM) cantilevers observed under either a scanning electron microscope (SEM)[36–39] or optical microscope[40, 41] to a broad range of approaches relying on the AFM for all measurements.

The ideal testing method would be simple and rapid; provide reliable and accurate results; and be applicable to a wide range of materials tested in a variety of different environments. The best available universal testing machines have a minimum force resolution of 50 nN, which limits their use for testing individual nanofibres. MEMS force sensors are more accurate, but their use requires either *in situ* SEM[32, 33] or the sensor needs to be glued to the fibre after mounting onto the MEMS testing platform.[34, 35] These processes are cumbersome, creating a long downtime between samples, and have not been demonstrated for testing in liquid environments.

The AFM has been a popular tool for nano-mechanical measurements since these instruments incorporate both force and distance sensors and can operate in air, liquids and vacuum. Although there are a vast range of commercial AFMs, none are specifically designed for tensile testing of nanofibres. Consequently, there are many methods for measuring mechanical properties by AFM. The most common approach is to move the cantilever perpendicular to the plane of the substrate with the measured cantilever deflection providing normal force such as nanoindentation[42, 43] or bending of a horizontally suspended nanofibre[44–49] to determine the material's Young's modulus or yield strength. Breaking strength and elongation at break are usually not measurable when using this geometry because the vertical range of motion for most AFM's is limited to a few micrometres.

A limited number of studies have used the horizontal motion of an AFM cantilever to measure the mechanical properties of nanofibres. The horizontal range of motion of most AFMs is at least an order of magnitude larger than the vertical range. When a fibre is mounted appropriately, it can be stretched to failure and provide the breaking strength and elongation at break in addition to the elastic and yield properties.[50] The two major difficulties arising with

the mechanical testing of individual nanofibres via this lateral loading by AFM are: the accurate and convenient calibration of the spring constant for lateral deflection of the AFM cantilever; and, the locating of individual fibres where they can be tested without slipping. The calibration of the lateral force of AFM cantilevers is still a matter of debate despite lateral force measurements being produced with the AFM for almost 25 years.[51, 52] Previously described methods for manipulation of individual fibres and fixing them at two points are both time consuming,[53–56] and prone to add defects to the fibres.

Here we describe a complete and simple approach to the preparation and tensile testing of individual electrospun nanofibres using an AFM. We introduce a method for fixing individual nanofibres across a gap that does not require additional handling of the fibres. We use the lateral movement of the AFM cantilever to enable tensile testing of the suspended fibres to high strains and apply the lateral force calibration method proposed by Liu and co-workers[57] because of its geometric similarity to the fibre test. We further expand the calibration method to account for the inherent non-linearity of the AFM sensor and variable fibre / cantilever tip contact point. Errors in the determination of stress and strain are given. The developed method is applied to a range of electrospun polymers in both air and liquid to demonstrate the versatility of the technique. These studies reveal unique process and size dependent mechanical properties of electrospun polymers.

2 Materials

Dimethylformamide (DMF), and tetrahydrofuran (THF), were obtained from AJAX Finechem. Buffer of pH 3 was prepared by mixing a ratio of 0.1 M citric acid (Sigma-Aldrich) and 0.2 M disodium hydrogen phosphate heptahydrate (Fluka).[58] Poly(acrylic acid) (PAA) (M_w ~450,000 g/mol) was purchased from Polysciences, Polystyrene, (PS) (Austrex 103) was supplied by

Polystyrene Australia. Poly(styrene-b-isobutylene-b-styrene) (SIBS) was a gift from Boston Scientific. All chemicals were used as received. Aqueous solutions were prepared using Milli-Q water (resistivity of 18.2 MΩ cm^{-1}). The glues used were UV-curable (DYMAX 425:light weld), epoxy (Araldite super strength) or nail polish (Sally Hanson).

3 Experimental

3.1 Electrospinning nanofibres

A syringe with an internal diameter of 150 μm (Dispense Tips, Nordson EFD) and high voltage power supply (Gamma High Voltage ES-30) were used for electrospinning. The details of the electrospinning conditions for each polymer are included in Table 1.

Table 1.Electrospinning parameters for the materials used.

Material	Voltage (kV)	Polymer concentration (%w/v)	Solvent	Syringe - collector distance (mm)	Atmosphere	Flow rate (ml/hr)
PS	10	10	DMF	180	Air	0.15
SIBS	20	15	THF	100	Air	0.4
PAA	10	8	H_2O	180	N_2	0.2

The fibres were electrospun onto TEM grids with parallel bars (Gold, Gilder Grids).[59] The space between the bars acts as a trench over which the fibres were suspended. During electrospinning, the TEM grids were positioned between parallel ground electrodes which resulted in electrospun fibres stretching between the electrodes during deposition producing fibres that were aligned perpendicular to the bars of the TEM grid.[60] Some of the PAA nanofibres were chemically crosslinked by exposure to UV radiation as described previously.[61]

3.2 Fixing the individual nanofibres to the TEM grid

The electrospun fibres were glued to the bars of the TEM grid with UV-curable adhesive (Figure 1). The glue was applied using a ~10 μm diameter glass fibre obtained from glass wool as a 'paint brush'. The placement of the glass fibre paint brush was achieved with a MarzhauserWetzlar DC-3K micromanipulator. Contact made between the glue droplet and a bar of the TEM grid caused the glue to wick along the metallic bars. The spreading glue engulfed the nanofibre such that UV-curing of the glue fixed the nanofibre to the bar.

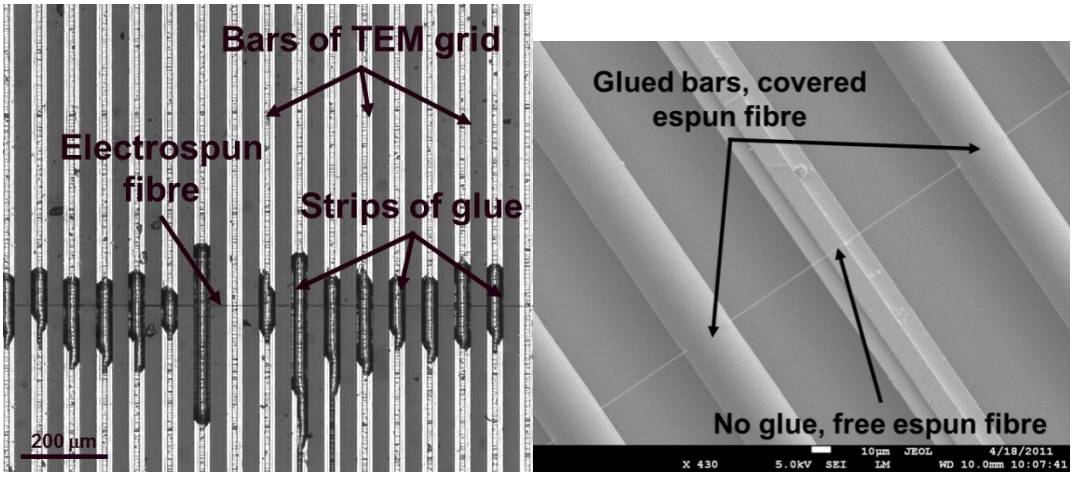

Figure 1. (left) An optical microscope image of a single electrospun SIBS fibre lying perpendicular to the (light grey) bars of a TEM grid with UV-curable glue to hold it suspended across the (dark grey) gaps between the bars. The bars without glue were used as sites to image the fibre and determine its dimensions. (right) SEM image of an electrospun PAA fibre spanning the bars of a TEM grid with and without glue holding the nanofibre in place.

3.3 Tensile testing of Nanofibres

3.3.1 Instrumentation

A JPK Nanowizard II AFM mounted on a Nikon TE 300/2000 inverted optical microscope was used. Rectangular AFM cantilevers with a range of stiffnesses were obtained from MikroMasch. SEM images were obtained with a JEOL JSM7500FA with samples sputter coated with gold before imaging.

3.3.2 AFM cantilever lateral force calibration

The calibration method used here was adapted from that described by Liu *et al.*[57] Glass fibres with radii of less than 1 μm and lengths of more than 150 μm were extracted from an Advantec GA-55 binder free glass fibre filter. Individual fibres were positioned over the edge of a glass slide using a micromanipulator then glued in place using epoxy. SEM was used to determine the dimensions of the glass fibre. The AFM cantilever tip's apex was used to laterally deflect the glass fibre. The glass fibre was repeatedly caught, bent and released by scanning the cantilever laterally back and forth perpendicular to the glass fibre's length. During lateral scanning the z-position variation (vertical height) of the cantilever was less than 50 nm per scan.

The force (F) needed to deflect a glass fibre a distance (Δy) is obtained from: [57, 62]

$$F = \frac{3Er^4}{4L^3}\Delta y \quad (1)$$

where E is the Young's modulus of glass (68 GPa[57]), r is the radius of the glass fibre, and L is the distance between the fixed end of the glass fibre and the point of contact with the AFM cantilever tip. Experimentally, the glass fibre deflection, Δy, is varied as the lateral photodetector response, V_l, is measured. When $\Delta y << L$ as is the case here, the lateral conversion factor (α_l) in units of μN/V is given by:

$$\alpha_l = \frac{F}{\Delta V_l} = \frac{3Er^4}{4L^3} \times \frac{\Delta y}{\Delta V_l} \quad (2)$$

The response of photo sensitive detectors (PSD) as used in an AFM are known to be nonlinear with respect to cantilever deflection.[63–65] Unlike many AFM methods that avoid the nonlinear

response by measuring over a small region of the PSD, the method used here often required a large range of the PSD due to the availability of cantilevers with the appropriate compliance. For all of the results reported here, the effects of nonlinearity were reduced by fitting the sensitivity over the full PSD range to a second degree polynomial and then normalising the measured data. This approach reduced the maximum difference in α_l from 30% to 2.7% over the full PSD range.

3.3.3 Effect of tip height on the lateral conversion factor

The height of contact on the cantilever tip apex from the glass fibre determines the torque applied to the cantilever and the degree of cantilever twist. A schematic diagram depicting the total tip height (h), the tip height from its base (ie. cantilever) to the glass fibre catching point (h_{sb}), and, the tip height from its apex to the glass fibre catching point (h_{se}) is shown in Figure 2. The distinction between h_{se} and h_{sb} is clarified here because h_{se} is easily measured.

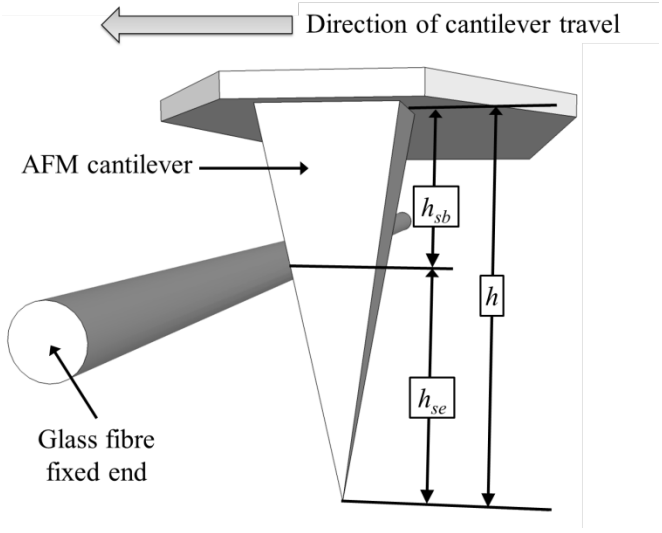

Figure 2. Schematic diagram of an AFM cantilever moving from right to left and coming into contact with a glass fibre, depicting the tip height (h) which is composed of the height of the glass fibre contact point measured from the cantilever (h_{sb}), and, measured from the tip apex (h_{se}).

A fixed value of h_{se} across all experiments was chosen to standardise the testing method. In considering the most suitable tip height it was realised that when the fibre is caught close to the tip's end the fibre frequently slipped off whilst being stretched. The most likely cause of the fibre slipping off is the relatively small contact area between the fibre and the tip, resulting in a small fibre-tip adhesion. In contrast, setting the catching height too close to the cantilever results in small torques and unacceptably large experimental error in force F. Consequently, h_{se} needs to be as small as possible without slipping. A h_{se} value of 4 μm was found to meet this requirement and was subsequently used for both calibration and testing of nanofibres.

3.3.4 Determination of fibre dimensions.

The length of the nanofibre between anchor points was measured using the optical microscope of the AFM. The cross sectional areas of the fibres were estimated by imaging them with the AFM in tapping mode at sites where they crossed a bar without glue. This approach is convenient, but likely over estimates the fibres cross-sectional area as the AFM is unable to image between the fibre and the substrate. By assuming an elliptical cross-section, the over estimation in area is less than 14%.

3.3.5 Laterally stretching an individual nanofibre with an AFM tip

Initial contact of the apex of the AFM cantilever tip with the nanofibre was achieved by laterally scanning for tip-fibre contact by lowering the cantilever by 1 μm steps. Once initial contact was observed, the tip was moved laterally away from the fibre and then lowered a further distance of 4 μm to set the fibre catching height. The 1 μm steps were carried out with the stepper motor while all other movements were achieved with the piezo motor. The cantilever was then scanned laterally over a total distance of 90 μm, typically at a speed of 1.8

μm/s, dragging the nanofibre with it (Figure 3). The z-piezo of the AFM head was held constant during lateral scanning. The resulting data was captured using the real time data scanner within the JPK control software. The tests were conducted in air or liquid as indicated.

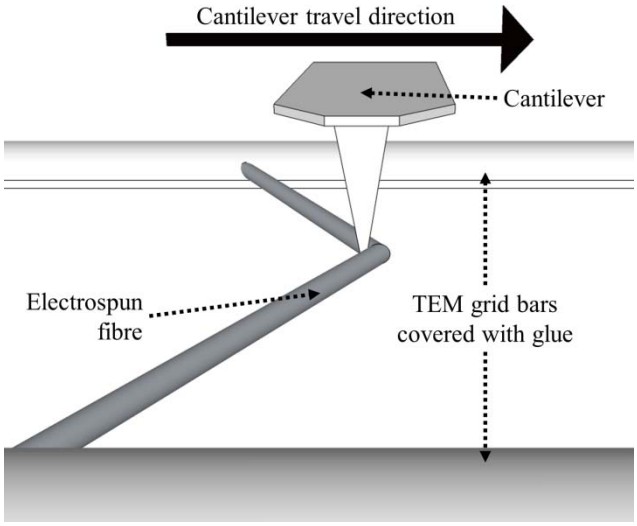

Figure 3. Schematic diagram of an AFM cantilever laterally scanning and dragging an electrospun fibre that is glued at both ends to the bars of a TEM grid.

3.4 Micro-Raman spectroscopy

Micro-Raman spectroscopy was used to determine if there was any polymer orientation within the PS nanofibres.[66, 67] The Raman microscope used was a Horiba JobinYvon HR800. Spectra were taken with a HeNe laser, polarised 500:1 at an excitation wavelength of 632.81 nm. A mat of aligned PS fibres was positioned at either 0^{o} or 90^{o} to the plane of polarisation of the incident laser. The Raman spectra were normalised to the peak at 620 cm^{-1} to observe the relative change in intensity of the peaks at 1000 and 1031 cm^{-1}.

3.5 Bulk SIBS testing

Hot pressed SIBS sheets were cut into strips (2.1 mm thick, 10 mm wide). These strips were subjected to cyclic tests at a strain rate of 4.5%/s using an INSTRON universal testing machine

with a grip spacing of 100 mm. Permanent strain refers to the strain immediately following a test cycle and does not allow for viscoelastic recovery.

4 Results and Discussion

4.1 Lateral conversion factors of cantilevers used.

The experimentally determined values of α_l at a V_l of 0 V for the cantilevers used are listed in Table 2. The reported numbers are the average of the α_l values taken over a range of values of L with the reported uncertainty being the standard deviation (SD) of that data set. Additional errors were estimated by Liu *et al.* to give a combined theoretical maximum uncertainty in α_l of ±16%.[57] The experimentally determined SD of α_l for each cantilever (3.2% to 15%) were typically less than this predicted maximum uncertainty (as detailed in Table 2).

Table 2. Values of experimentally determined α_l and SD at 0 V V_l baseline in air for 4 cantilevers with different manufacturer reported values of normal stiffness, k_n. The SD was determined from a minimum of 10 repeat measurements.

Cantilever no.	k_n (N/m)	α_l (μN/V) (air)
1	0.05	0.11 ± 15%
2	0.08	0.32 ± 15%
3	0.6	1.4 ± 10%
4	1.75	3.5 ± 3.2%

4.2 Force calculations for 3-point tensile tests

The lateral force measured from the rotation of the cantilever free end (F_l) versus cantilever travel (x) curves that are generated from a 3-point mechanical test (Figure 4) require some

consideration before they can be converted into stress strain curves for the tested fibre. The fibre's mechanical properties and dimensions have a strong effect on the way that it will respond to a 3-point mechanical test. A schematic diagram showing the fibre length and both the lateral force and fibre tensile force measured during fibre stretching by an AFM cantilever is presented in Figure 5. In the three point configuration, a fibre with a high elastic modulus (E > ~100 GPa) and low aspect ratio (length: diameter< 5:1) will show purely bending behaviour.[53, 68] In these cases the 3-point loading produces a linear F_l- x curve in the elastic region. Fibres with a low modulus (E < ~10 GPa) and a high aspect ratio (> 30:1) are dominated by the axial tensile stretching of the fibre.[56, 69, 70] Tensile stretching tests in a 3-point configuration, like those conducted here, result in a non-linear F_l- x curve in the elastic region.

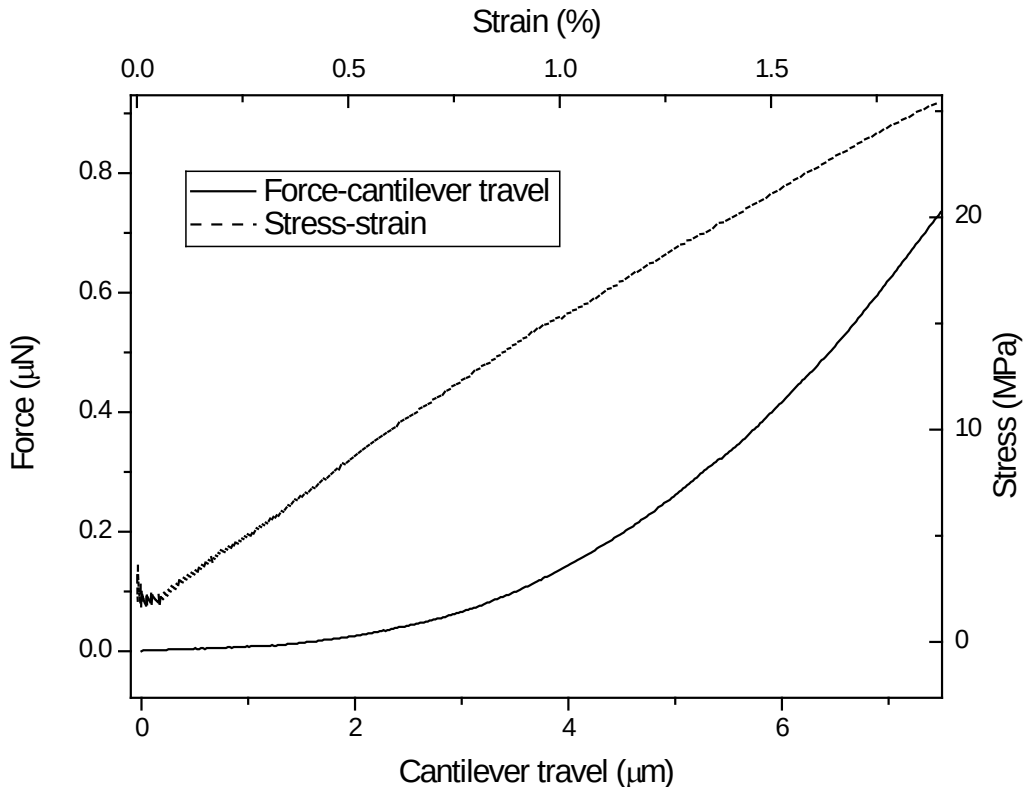

Figure 4. Typical F_l - x curve and the corresponding stress-strain curve in the elastic region for a single PS nanofibre.

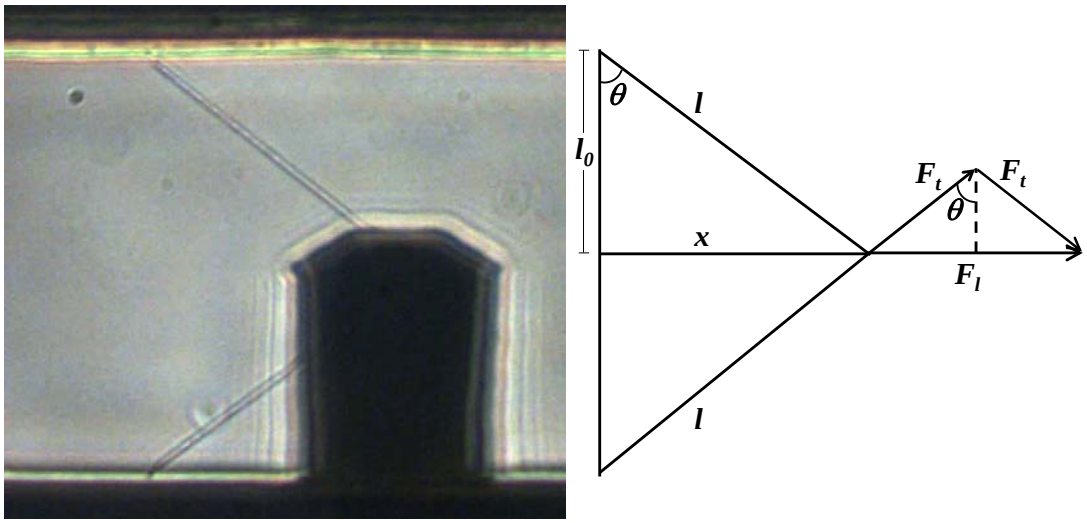

Figure 5. (left) Optical microscope image of a PS nanofibre being stretched by an AFM cantilever and (right) a schematic diagram showing the dimensions and resulting force. F_l is the force measured at the cantilever, F_t is the tensile force acting on each half of the fibre, $2l_0$ and $2l$ are the initial and final length of the fibre and x is the cantilever travel distance.

All of the electrospun fibres measured here have dimensions and properties that fall in the range for which the 3-point mechanical test can be treated as tensile stretching. Aspect ratios are greater than 60:1 and the modulus of the polymer fibres is always less than 4 GPa. Using the tensile stretching model rather than a bending model to fit the data is also supported by the observed non-linearity of the elastic region of the F_l - x curves for all nanofibres studied (Figure 4). Assuming a tensile stretching model the following expressions can be derived for the fibre tensile stress (σ) and strain (ε) as illustrated in Figure 5:

$$\sigma = \frac{F_l}{2A\sin(\theta)} \qquad (1)$$

$$\varepsilon = \frac{\left(\frac{x}{\sin(\theta)}\right) - l_0}{l_0} \qquad (2)$$

$$\tan(\theta) = \frac{x}{l_0} \qquad (3)$$

where F_l is the lateral force felt at the cantilever (directly converted from the measured ΔV_l with α_l), A is the cross-sectional area of the fibre, x is the cantilever travel from the initial point of catching the fibre, θ is the angle between the stretched and initial position of the fibre and l_o is half the initial length of the fibre as shown schematically in Figure 5. These equations were used to convert the experimentally obtained force versus cantilever travel curves to stress-strain curves. The stress-strain curves were then used to obtain the fibre's E along with the yield and breaking stresses, and, the yield and breaking strains. At very small strains (<0.1 %) the stress strain curve shown in Figure 4 shows a large error since angle θ approaches zero (equation 1). This factor is typical of all the mechanical tests carried out by the lateral loading method and means that the very small strain mechanical properties could not be accurately determined. The use of this tensile only model was confirmed by macro scale mechanical tests performed in both testing configurations on fibres with similar Young's moduli and aspect ratios to the nanofibres.

4.3 Applications of the method

4.3.1 Observation of high ductility in normally brittle polymers

A typical stress-strain tensile test result for PS and PAA electrospun fibres are presented in Figure 6 and Figure 9. The curves show a yield-like transition followed by extensive post-yield drawing. Remarkably, the breaking strain measured for the glassy polymer PS and PAA nanofibres respectively, at 85% ± 15% and 150% ± 16%, greatly exceeds that of bulk PS at 1 – 4%[71] and bulk dry PAA at ~4 %. In contrast, the Young's modulus of electrospun PS nanofibres of 1.3±0.10 GPa were of the same order of magnitude as that for bulk PS. Over the

range of nanofibre cross-sectional areas tested here, there was no significant effect of fibre diameter on the elongation at break and Young's moduli. Other reports,[38, 72] however, have suggested a critical size corresponding to a brittle-ductile transition in PS nanofibres. The small dimensions of the nanofibres are thought to suppress the fracture mechanisms that cause brittleness in bulk PS,[38] although the reasons for this phenomenon remain unclear.

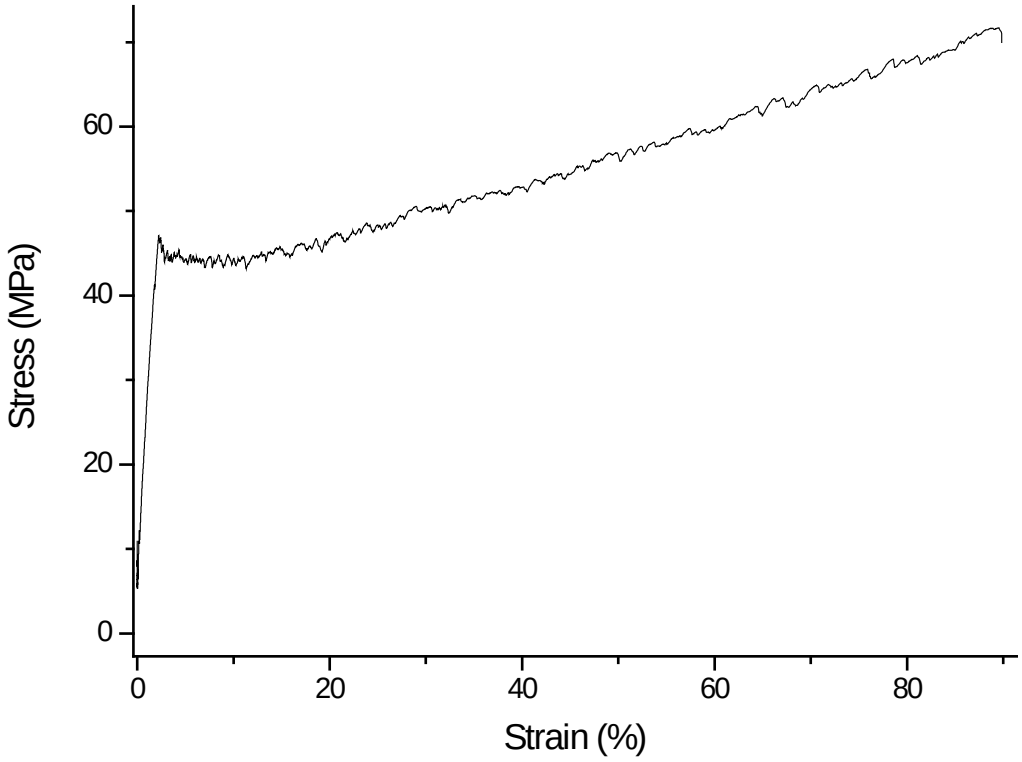

Figure 6. Stress-strain diagram from an AFM 3-point tensile test of an individual PS nanofibre.

Electrospinning of polymers is known to induce polymer chain orientation and highly oriented bulk PS has been shown to be highly ductile. Brittle fracture in bulk, isotropic PS (at room temperature) is associated with cracks initiating from crazes that form from extensive local yielding, typically near stress-concentrating defects. For low entanglement density polymers like PS, polymer orientation is known to suppress craze formation and reduce the extent of

localised yielding. In fact, PS shows a brittle to ductile transition upon polymer chain alignment for both macroscopic specimens[73] and sub- millimetre diameter fibres.[74–76] Polymer chain orientation can be induced by the electrospinning process[66, 77] and the PS within the nanofibres produced here were confirmed to have some degree of axial alignment by polarised Raman spectroscopy (Figure 7). For Raman spectroscopy of PS, the peak at 620 cm^{-1} results from a ν_{6b} vibration of the phenyl group and is assumed to be insensitive to orientation.[78] In contrast, the peaks at 1001 and 1031 cm^{-1} result from ν_{12} and ν_{18a} vibrations of the phenyl group and are highly sensitive to orientation effects.[78] Hence, the ratio of intensity of the peaks at 1001 and 1031 cm^{-1} to the peak at 620 cm^{-1} can be used to determine if main chain orientation occurs. The difference in the peak intensity ratio for spectra taken at different angles to the plane of polarisation shown in Fig. 7 confirms a high degree of main chain alignment along the fibre direction in the electrospun PS nanofibres.

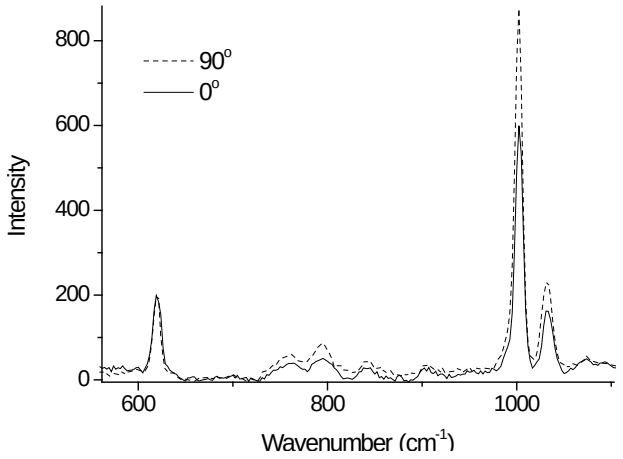

Figure 7. Raman spectra of aligned PS nanofibres at 0^o and 90^o to the plane of polarisation.

While the high degree of polymer orientation in the electrospun PS fibres likely contributes to their unusual ductility, other explanations may also be relevant. For example, the elimination of stress concentrating defects will reduce the occurrence of craze formation and crack propagation. Carefully formed bulk PS samples with nearly perfect surfaces and free of trapped

foreign particles have been shown to achieve a plastic strain of 5-8% and display extensive crazing throughout.[79] However, the observed plastic strain of PS nanofibres in the present study was greater than 90% and cannot singly be attributable to the reduction in stress concentrations.

Another possible cause of the high ductility is a predicted decrease in glass transition of PS in confined films and fibres. A brittle (craze formation) to ductile (shear yielding) transition has been predicted due to the increased mobility of polymer chains in PS films of thicknesses below 100 nm.[80, 81] In the present study it is noted that the Young's modulus of the PS fibres indicates that they are still a polymer glass. Furthermore, Raman spectroscopy[78] indicated that the polymer is orientated long after being produced, implying that the polymer is well below its glass transition and has not undergone substantial recovery. Hence, it is unlikely that the PS in the form of the fibres presented here has a sufficient increase in mobility to change the yielding mechanism.

In a phenomenological study on electrospun PS mats, Asran and co-workers[72] noted a difference in deformation mechanism depending upon the diameter of their nanofibres. Crazing occurred in stretched PS fibres with a diameter larger than 225 nm, while necking was noted in stretched PS fibres with a diameter less than 225 nm. SEM analysis of stretched PS fibres of the present study (Figure 8) at ~350 nm diameter did not show any signs of crazing or necking throughout their entire strain range. Additionally, there did not appear to be any signs of damage or buckling at the contact point made by the AFM tip at the centre of the fibre's length so that localised yielding does not appear to have occurred. Clearly, the PS fibres exhibit high ductility without massive localised yielding in contrast to the findings of Asran and co-workers. Differences in electrospinning conditions and the degree of molecular orientation are likely reasons for the differing observations in the two studies.

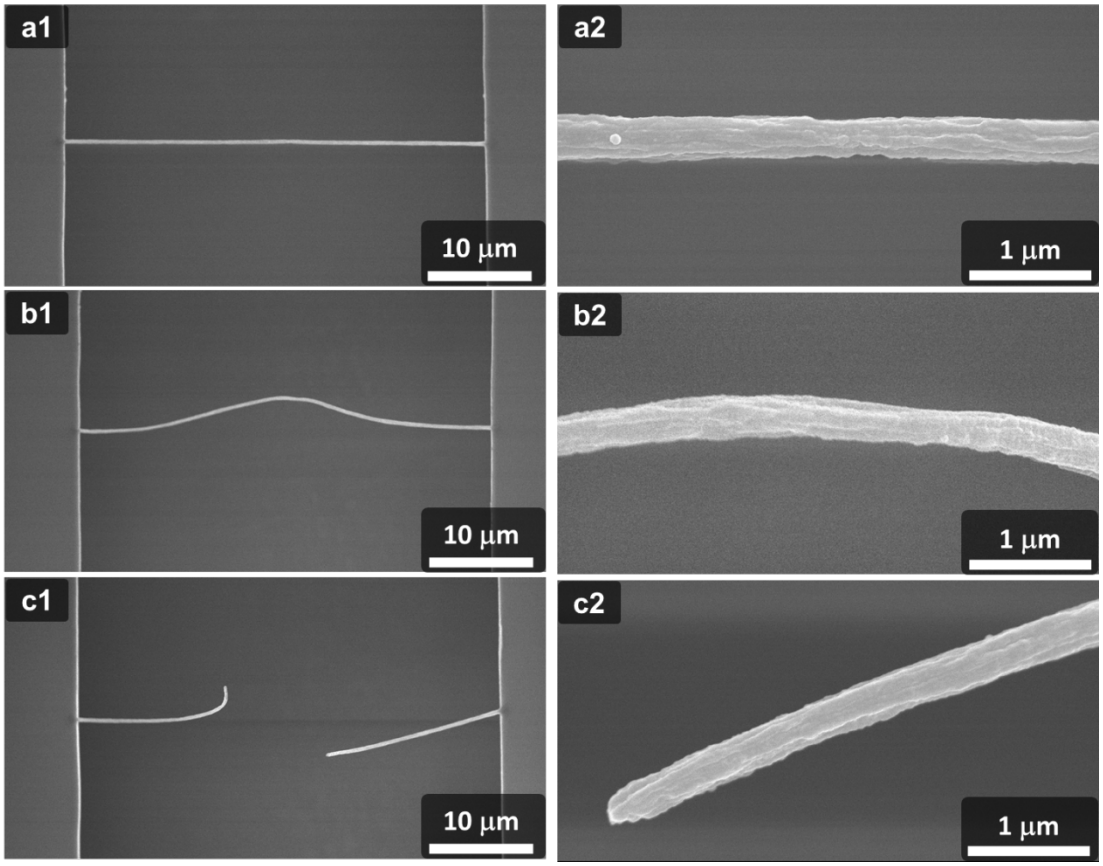

Figure 8. SEM of PS nanofibres that were stretched with the AFM to (a1 & a2) 4.3 %, (b1 & b2) 22 %, and (c1 & c2) 25 % strain, a2 and b2 were taken at the midpoint between the TEM grid bars to look for any impact of the AFM tip while c2 is the breaking point of the fibre.

4.3.2 Differentiation of PAA fibres with different cross-link densities, and in liquid environments

A decrease in ductility with increasing crosslink densities was easily resolved by the AFM three-point mechanical tests for PAA nanofibres (Figure 9). Exposure of the PAA nanofibres to UV in an inert nitrogen environment (UVN_2) for varying times was used to induce crosslinking and increased exposure time was observed to decrease the ductility of the PAA nanofibres. The crosslinking of polymer chains reduces their mobility which limits the uncoiling and slipping associated with post yield drawing and ductility. Substantial strain

hardening was resolved by the AFM tests on samples with relatively high crosslink densities is also typical of an increase in crosslink density for glassy polymers.[80]

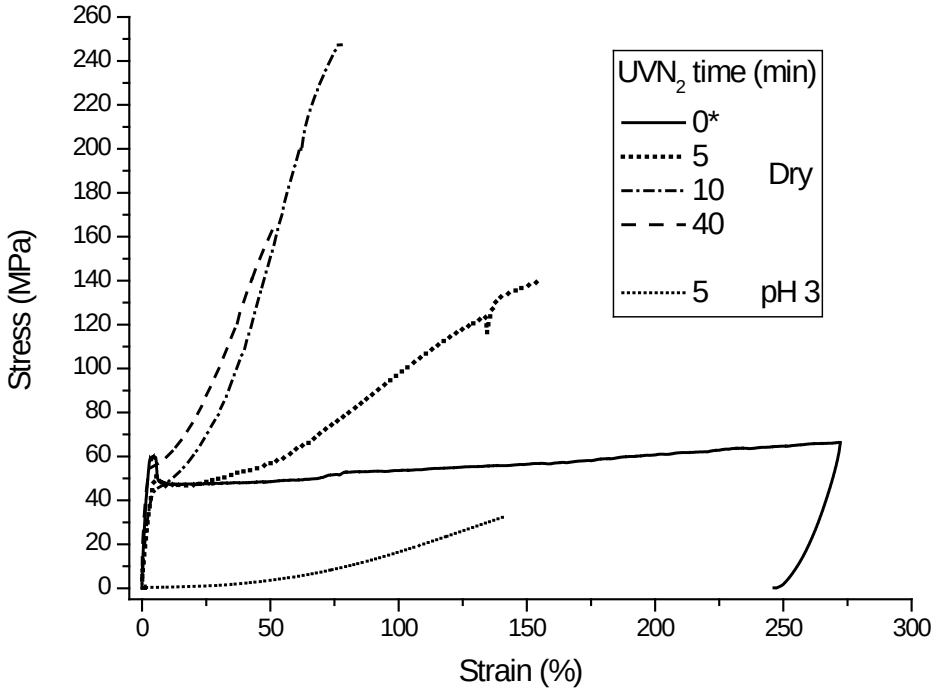

Figure 9. Stress-strain curves from an AFM 3-point tensile test of PAA nanofibres UVN_2 treated for 0 to 40 minutes. The crosslink density within the fibres increases with UVN_2 radiation time. *The curve for the 0 minute UVN_2 PAA curves back on itself because the fibre did not break before the AFM reached its full scan limit and began to unload the fibre.

The tensile test approach introduced here was also demonstrated in a liquid environment (Figure 9). As expected, the Young's modulus of a crosslinked PAA nanofibre solvated by pH 3 buffer (30±4.9 MPa) was 2 orders of magnitude lower than that observed for a dry PAA nanofibre (1.3±0.10 GPa) of the same crosslink density. The *E* of the PAA hydrogel nanofibres measured here and previous reports of their swelling[61] are comparable to low swelling hydrophobically modified hydrogels.[82]

4.3.3 Resilience of thermoplastic elastomer nanofibres

The AFM tensile test was also assessed for evaluating the resilience to high strain of thermoplastic elastomer nanofibres through load/unload cycling to high strain. Typical cyclic tensile results for a SIBS nanofibre and bulk SIBS are presented in Figure 10. The SIBS samples were stretched to the maximum strain allowed by the range of lateral motion of the AFM head and then unloaded. The nanofibre SIBS sample showed a very large load/unload hysteresis and some permanent plastic deformation (~18%) during the first cycle. Second and subsequent load/unload cycles were similar to the first unloading with considerably higher resilience than the first cycle and negligible plastic deformation. In comparison to the nanofibres, bulk SIBS exhibits a smaller decrease in stress at equivalent strains when comparing the first to subsequent cycles although the extent of plastic deformation in the first cycle (~16%) was similar. In fact, the stress-strain curves for the bulk SIBS are remarkably similar to those of the nanofibre SIBS sample after the first cycle except at high strain (Figure 10b insert).

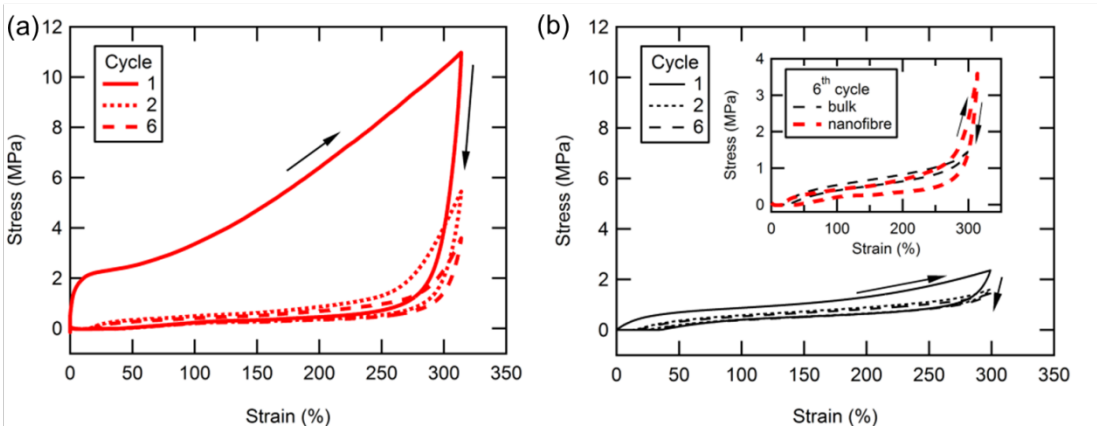

Figure 10. Cyclic stress-strain curves for (a) SIBS electrospun fibres, and, (b) bulk SIBS. The inset shows a comparison of the SIBS nanofibre and bulk SIBS sample tested on the 6th load / unload cycle.

It is apparent that stretching the as-spun SIBS nanofibres removes the unusual mechanical properties observed in the first stretching cycle. The as-spun SIBS nanofibres are much stiffer

(Young's modulus of 59±27 MPa) than bulk SIBS (E~ 3 MPa) but show similar moduli (2.0±0.1 MPa) to the bulk for subsequent stretching cycles. In fact, the tensile properties of the SIBS nanofibre during the first stretch resemble those of thermoplastic elastomers that have a higher volume fraction of glassy polymer resulting in a continuous phase of glassy polymer rather than the equilibrium isolated spherical domains of the SIBS used here.[83, 84] It is possible that the electrospinning process produces an unusual, non-equilibrium microstructure of continuous PS phase with dispersed rubbery domains. During tensile extension, these glassy PS regions yield and break-up to form a discontinuous phase which then resembles the typical equilibrium structure of SIBS. Subsequent loading is then dominated by the continuous rubbery phase giving mechanical behaviour typical of bulk SIBS.

5 Conclusions

Overall, a complete method for measuring the tensile properties of individual polymer nanofibres, from calibration to execution, has been developed. This approach is achievable at minimal cost by any lab with access to an AFM. The usefulness of such a technique was highlighted by the unexpected tensile curves obtained for common polymer systems and new insights gained into nano-mechanical behaviour.

The method used to prepare and measure the mechanical properties of the nanofibres benefited from being able to acquire data at a high sampling rate, obtain complete tensile stress-strain curves, conduct tests in air or liquid, and a relatively simple sample preparation which required no physical handling of the individual fibres. Fibres with elastic moduli ranging from 1 MPa to 1 GPa, breaking strengths ranging from 1×10 MPa to 1×10^2 MPa, and strains up 300% were observed. Larger breaking strains are possible by increasing the range of travel of the AFM scanning system, or, by using a TEM grid with a smaller bar spacing. Due to stress

concentration within the fibre at the glued ends, and the cantilever fibre contact, the observed stress should be considered as a lower limit only.

For the measurement of stress, the main sources of error were determined to relate to the inaccuracies in determining the nanofibre cross-sectional area, and the calibration of the lateral spring constant of the cantilever. Consequently, the variation in modulus and strength values for the nanofibres was considerable. Measurement of strain was significantly more accurate than stress as neither cross-sectional area or lateral spring constant are used for its determination. While less accurate than macro-scale testing, the AFM approach presented here was still able to readily distinguish between glassy and rubbery polymers on the basis of their moduli values and could distinguish fibres of the same material with increasing cross-link density based on their breaking strain and strain hardening.

The tensile properties of many electrospun nanofibres are substantially different to those for bulk isotropic samples of the same polymer. Specifically, the typically brittle glassy polymers PS and PAA are ductile under tension for the spinning conditions used here. In addition, the elastomer SIBS exhibited a much higher modulus than bulk SIBS when it is first stretched possibly due to the formation of a non-equilibrium microstructure during electrospinning.

6 Acknowledgements

The authors acknowledge the financial support of the Australian Research Council through the Centre of Excellence and Fellowship schemes and the Australian National Fabrication Facility. The authors also acknowledge use of the facilities and the assistance of Tony Romeo at the UOW Electron Microscopy Centre.

7 References

1. H.S. Yoo, T.G. Kim, and T.G. Park, Advanced Drug Delivery Reviews **61**, 12, 1033–42 (2009).

2. S. Chakraborty, I.-C. Liao, A. Adler, and K.W. Leong, Advanced Drug Delivery Reviews **61**, 12, 1043–54 (2009).

3. W. Cui, Y. Zhou, and J. Chang, Science and Technology of Advanced Materials **11**, 1, 014108 (2010).

4. J. Venugopal and S. Ramakrishna, Applied Biochemistry and Biotechnology **125**, 3, 147–58 (2005).

5. T.J. Sill and H. a von Recum, Biomaterials **29**, 13, 1989–2006 (2008).

6. S.G. Kumbar, R. James, S.P. Nukavarapu, and C.T. Laurencin, Biomedical Materials (Bristol, England) **3**, 3, 034002 (2008).

7. M. Khil, D.-I. Cha, H.-Y. Kim, I. Kim, and N. Bhattarai, Journal of Biomedical Materials Research. Part B, Applied Biomaterials **67**, 2, 675–9 (2003).

8. A. Merzlyak, S. Indrakanti, and S.-W. Lee, Nano Letters **9**, 2, 846–52 (2009).

9. W.J. Li, C.T. Laurencin, E.J. Caterson, R.S. Tuan, and F.K. Ko, Journal of Biomedical Materials Research **60**, 4, 613–621 (2002).

10. C.P. Barnes, S. a Sell, E.D. Boland, D.G. Simpson, and G.L. Bowlin, Advanced Drug Delivery Reviews **59**, 14, 1413–33 (2007).

11. R. Murugan and S. Ramakrishna, Tissue Engineering **12**, 3, 435–47 (2006).

12. J. Xie and C.-H. Wang, Pharmaceutical Research **23**, 8, 1817–26 (2006).

13. Z. Lin, L. Ji, and X. Zhang, Electrochimica Acta **54**, 27, 7042–7047 (2009).

14. J. Chen, B. Li, J. Zheng, J. Zhao, H. Jing, and Z. Zhu, Electrochimica Acta 2010, (2011).

15. M.-S. Wu, Y.-H. Ou, and Y.-P. Lin, Electrochimica Acta **55**, 9, 3240–3244 (2010).

16. K. Ghanbari, M. Mousavi, and M. Shamsipur, Electrochimica Acta **52**, 4, 1514–1522 (2006).

17. K. Pawlowski, Polymer **44**, 4, 1309–1314 (2003).

18. D. Blond, W. Walshe, K. Young, F.M. Blighe, U. Khan, D. Almecija, L. Carpenter, J. McCauley, W.J. Blau, and J.N. Coleman, Advanced Functional Materials **18**, 17, 2618–2624 (2008).

19. T. Uyar, R. Havelund, Y. Nur, J. Hacaloglu, F. Besenbacher, and P. Kingshott, Journal of Membrane Science **332**, 1-2, 129–137 (2009).

20. H.S. Lim, J.H. Baek, K. Park, H.S. Shin, J. Kim, and J.H. Cho, Advanced materials **22**, 19, 2138–41 (2010).

21. M. Naebe, T. Lin, M.P. Staiger, L. Dai, and X. Wang, Nanotechnology **19**, 30, 305702 (2008).

22. N. Detta, A.A. El-Fattah, E. Chiellini, P. Walkenström, and P. Gatenholm, Journal of Applied Polymer Science **110**, 1, 253–261 (2008).

23. H. Jin, Biomaterials **25**, 6, 1039–1047 (2004).

24. A. Pedicini and R.J. Farris, Polymer **44**, 22, 6857–6862 (2003).

25. M. Li, M. Mondrinos, M. Gandhi, F. Ko, a Weiss, and P. Lelkes, Biomaterials **26**, 30, 5999–6008 (2005).

26. C.R. Carlisle, E. a Sparks, C. Der Loughian, and M. Guthold, Journal of Thrombosis and Haemostasis **8**, 5, 1135–8 (2010).

27. N.E. Hudson, J.R. Houser, E.T. O'Brien, R.M. Taylor, R. Superfine, S.T. Lord, and M.R. Falvo, Biophysical Journal **98**, 8, 1632–40 (2010).

28. E. Tan and C. Lim, Composites Science and Technology **66**, 9, 1102–1111 (2006).

29. S.Y. Chew, T.C. Hufnagel, C.T. Lim, and K.W. Leong, Nanotechnology **17**, 15, 3880–3891 (2006).

30. E.P.S. Tan, S.Y. Ng, and C.T. Lim, Biomaterials **26**, 13, 1453–6 (2005).

31. Z. Chen, B. Wei, X. Mo, C.T. Lim, S. Ramakrishna, and F. Cui, Materials Science and Engineering: C **29**, 8, 2428–2435 (2009).

32. B.A. Samuel, M.A. Haque, B. Yi, R. Rajagopalan, and H.C. Foley, Nanotechnology **18**, 11, 115704 (2007).

33. D. Jaeger, J. Schischka, J. Bagdahn, and R. Jaeger, Journal of Applied Polymer Science **114**, 6, 3774–3779 (2009).

34. M. Naraghi, S.N. Arshad, and I. Chasiotis, Polymer **52**, 7, 1612–1618 (2011).

35. M. Naraghi, I. Chasiotis, H. Kahn, Y. Wen, and Y. Dzenis, The Review of scientific instruments **78**, 8, 085108 (2007).

36. L.-Q. Liu, D. Tasis, M. Prato, and H.D. Wagner, Advanced Materials **19**, 9, 1228–1233 (2007).

37. E. Zussman, X. Chen, W. Ding, L. Calabri, D. a. Dikin, J.P. Quintana, and R.S. Ruoff, Carbon **43**, 10, 2175–2185 (2005).

38. R.J. Bailey, B. Cortes-Ballesteros, H. Zhang, C. Wang, and A.H. Barber, MRS Proceedings **1424**, mrsf11–1424–ss03–04 (2012).

39. F. Hang and A.H. Barber, Journal of the Royal Society, Interface / the Royal Society **8**, 57, 500–5 (2011).

40. J. Ji, B. Bar-On, and H. Daniel Wagner, Journal of the Mechanical Behavior of Biomedical Materials (2012).

41. E. Zussman, M. Burman, A.L. Yarin, R. Khalfin, and Y. Cohen, Journal of Polymer Science Part B: Polymer Physics **44**, 10, 1482–1489 (2006).

42. M.R. VanLandingham, J.S. Villarrubia, W.F. Guthrie, and G.F. Meyers, "Nanoindentation of polymers: An overview," in *Macromolecular symposia*, (John Wiley & Sons, 2001), pp. 15–44.

43. M.E. Dickinson and J.P. Schirer, Materials Today **12**, 7-8, 46–50 (2009).

44. J.-P. Salvetat, A.J. Kulik, J.-M. Bonard, G.A.D. Briggs, T. Stöckli, K. Méténier, S. Bonnamy, F. Béguin, N. a. Burnham, and L. Forró, Advanced Materials **11**, 2, 161–165 (1999).

45. J.-P. Salvetat, G. Briggs, J.-M. Bonard, R. Bacsa, A. Kulik, T. Stöckli, N. Burnham, and L. Forró, Physical Review Letters **82**, 5, 944–947 (1999).

46. J. Duvail, P. Retho, C. Godon, C. Marhic, G. Louarn, O. Chauvet, S. Cuenot, B. Nysten, L. Dauginet-De Pra, and S. Demoustier-Champagne, Synthetic metals **135**, 329–330 (2003).

47. S. Lee, C. Tekmen, and W. Sigmund, Materials Science and Engineering A **398**, 1-2, 77–81 (2005).

48. L.M. Bellan, J. Kameoka, and H.G. Craighead, Nanotechnology **16**, 8, 1095–1099 (2005).

49. W. Wang and A.H. Barber, Journal of Polymer Science Part B: Polymer Physics **50**, 8, 546–551 (2012).

50. C.R. Carlisle, C. Coulais, M. Namboothiry, D.L. Carroll, R.R. Hantgan, and M. Guthold, Biomaterials **30**, 6, 1205–13 (2009).

51. C. Mate, G. McClelland, R. Erlandsson, and S. Chiang, Physical Review Letters **59**, 17, 1942–1945 (1987).

52. M. Munz, Journal of Physics D: Applied Physics **43**, 6, 063001 (2010).

53. B. Wu, A. Heidelberg, and J.J. Boland, Nature Materials **4**, 7, 525–529 (2005).

54. A. Heidelberg, L.T. Ngo, B. Wu, M.A. Phillips, S. Sharma, T.I. Kamins, J.E. Sader, and J.J. Boland, Nano Letters **6**, 6, 1101–6 (2006).

55. B. Wen, J. Sader, and J. Boland, Physical Review Letters **101**, 17, (2008).

56. D. Almecija, D. Blond, J.E. Sader, J.N. Coleman, and J.J. Boland, Carbon **47**, 9, 2253–2258 (2009).

57. W. Liu, K. Bonin, and M. Guthold, Review of Scientific Instruments **78**, 6, 063707 (2007).

58. T. McIlvaine, Journal of Biological Chemistry **49**, 183–186 (1921).

59. A. Gestos, P.G. Whitten, G.G. Wallace, and G.M. Spinks, Soft Matter **8**, 31, 8082 (2012).

60. M.K. Shin, S.I. Kim, S.J. Kim, S.-K. Kim, H. Lee, and G.M. Spinks, Applied Physics Letters **89**, 23, 231929 (2006).

61. A. Gestos, P.G. Whitten, G.M. Spinks, and G.G. Wallace, Soft Matter **6**, 5, 1045 (2010).

62. W.C. Young and R.G. Budynas, *Roark's formulas for stress and strain* (McGraw-Hill New York, 2002) , 7th ed.

63. E.C.C.M. Silva and K.J. Van Vliet, Nanotechnology **17**, 21, 5525–5530 (2006).

64. L.Y. Beaulieu, M. Godin, O. Laroche, V. Tabard-Cossa, and P. Gru□tter, Applied Physics Letters **88**, 8, 083108 (2006).

65. R.J. Cannara, M. Eglin, and R.W. Carpick, Review of Scientific Instruments **77**, 5, 053701 (2006).

66. M. V Kakade, S. Givens, K. Gardner, K.H. Lee, D.B. Chase, and J.F. Rabolt, Journal of the American Chemical Society **129**, 10, 2777–82 (2007).

67. S.M. Iconomopoulou and G. a Voyiatzis, Journal of Controlled Release□: Official Journal of the Controlled Release Society **103**, 2, 451–64 (2005).

68. A. Kis, D. Mihailovic, M. Remskar, A. Mrzel, A. Jesih, I. Piwonski, A.J. Kulik, W. Benoît, and L. Forró, Advanced Materials **15**, 9, 733–736 (2003).

69. D. a. Walters, L.M. Ericson, M.J. Casavant, J. Liu, D.T. Colbert, K. a. Smith, and R.E. Smalley, Applied Physics Letters **74**, 25, 3803 (1999).

70. Y.-J. Kim, K. Son, I.-C. Choi, I.-S. Choi, W. Il Park, and J. Jang, Advanced Functional Materials **21**, 2, 279–286 (2011).

71. J.E. Mark, Ed., *Physical Properties of Polymers Handbook* (Springer, 2007) , 2nd ed.

72. A.S. Asran, V. Seydewitz, and G.H. Michler, Journal of Applied Polymer Science **125**, 3, 1663–1673 (2012).

73. J.W. Curtis, Journal of Physics D: Applied Physics **3**, 10, 1413–1422 (1970).

74. R.D. Andrews, Journal of Applied Physics **25**, 10, 1223 (1954).

75. Y. Tanabe and H. Kanetsuna, Journal of Applied Polymer Science **22**, 6, 1619–1630 (1978).

76. Y. Tanabe and H. Kanetsuna, Journal of Applied Polymer Science **22**, 9, 2707–2711 (1978).

77. A. Baji, Y.-W. Mai, S.-C. Wong, M. Abtahi, and P. Chen, Composites Science and Technology **70**, 5, 703–718 (2010).

78. B. Jasse, R.S. Chao, and J.L. Koenig, Journal of Polymer Science: Polymer Physics Edition **16**, 2157–2169 (1978).

79. A.S. Argon and J.G. Hannoosh, Philosophical Magazine **36**, 5, 1195–1216 (1977).

80. H.G.H. van Melick, L.E. Govaert, and H.E.H. Meijer, Polymer **44**, 8, 2493–2502 (2003).

81. J. Forrest and J. Mattsson, Physical Review. E, Statistical Physics, Plasmas, Fluids, and Related Interdisciplinary Topics **61**, 1, R53–6 (2000).

82. S. Naficy, H.R. Brown, J.M. Razal, G.M. Spinks, and P.G. Whitten, Australian Journal of Chemistry **64**, 8, 1007 (2011).

83. J. Puskas, P. Anthony, M.E. Fray, and V. Altstadt, European Polymer Journal **39**, 10, 2041–2049 (2003).

84. R.F. Storey and B.J. Chisholm, Polymer **37**, 14, 2925–2938 (1996).